

Demonstration of molecular chirality discrimination by resonance Raman scattering

Mustafa Eginligil

iameginligil@njtech.edu.cn

Nanjing Tech University <https://orcid.org/0000-0002-4494-7066>

Shengkai Zhao

Nanjing Tech University

Balzhan Baltabayeva

Nanjing Tech University

Mingrui Zhang

Nanjing University

Jianmin Wang

Nanjing Tech University

Yufeng Hao

Nanjing University <https://orcid.org/0000-0001-7758-5244>

Wei Huang

Frontiers Science Center for Flexible Electronics, Xi'an Institute of Flexible Electronics and Xi'an Institute of Biomedical Materials & Engineering, Northwestern Polytechnical University

Article

Keywords: chiral molecules, resonance Raman spectroscopy, pseudo-Jahn-Teller effect, linearly polarized Raman

Posted Date: January 16th, 2024

DOI: <https://doi.org/10.21203/rs.3.rs-3770494/v1>

License:   This work is licensed under a Creative Commons Attribution 4.0 International License.

[Read Full License](#)

Additional Declarations: There is **NO** Competing Interest.

Demonstration of molecular chirality discrimination by resonance Raman scattering

Shengkai Zhao¹, Balzhan Baltabayeva¹, Mingrui Zhang², Jianmin Wang¹, Yufeng Hao^{2*}, Mustafa Eginligil^{1*}, Wei Huang^{1, 3, 4*}

¹Key Laboratory of Flexible Electronics (KLoFE) & Institute of Advanced Materials (IAM), School of Flexible Electronics (Future Technologies), Nanjing Tech University (NanjingTech); Nanjing, China.

²National Laboratory of Solid State Microstructures, College of Engineering and Applied Sciences, Collaborative Innovation Center of Advanced Microstructures, and Jiangsu Key Laboratory of Artificial Functional Materials, Nanjing University; Nanjing, China.

³Frontiers Science Center for Flexible Electronics (FSCFE) & Shaanxi Institute of Flexible Electronics (SIFE), Northwestern Polytechnical University (NPU); Xi'an, China.

⁴State Key Laboratory of Organic Electronics and Information Displays, Institute of Advanced Materials (IAM), Nanjing University of Posts & Telecommunications; Nanjing, China.

*Mustafa Eginligil, Yufeng Hao, Wei Huang

Email: ME: iameginligil@njtech.edu.cn; YH: haoyufeng@nju.edu.cn; WH: vc@nwpu.edu.cn

Keywords: chiral molecules, resonance Raman spectroscopy, pseudo-Jahn-Teller effect, linearly polarized Raman.

This PDF file includes:

Main Text

Figures 1 to 4

Table 1

Abstract

The pseudo-Jahn-Teller (PJT) effect, a direct indicator of molecular instability, can be the reason of sub-meV split degenerate electronic states that can be used to discriminate enantiomers. In the exemplar chiral molecule of camphor ($C_{10}H_{16}O$), the nondegenerate vibrational states were previously identified, but there has been no evidence of PJT states. Here, linearly polarized Raman measurements were employed to demonstrate the PJT states, with splitting of $1.8 \pm 0.2 \text{ cm}^{-1}$, for scattering by chiral centers on carbon ring of camphor. This observation is attributed to the symmetry reduction and chirality-dependent C_3 symmetry becoming intact by placing camphor on a SiO_2/Si substrate. The depolarization ratio, the noncoincidence effect, and the molecular chirality-dependent polarization rotation of the PJT states manifested a clear distinction between enantiomers. More importantly, quantification of chirality was possible based on the occupancy of the PJT states at the depolarized state, which is applicable to similar chiral molecules.

Significance Statement

The discrimination between enantiomers, detection, and quantification of chirality in molecules is challenging due to environmental effects. This experimental work demonstrated that doubly-degenerate pseudo-Jahn-Teller states in the exemplar chiral molecule of camphor in depolarized micro-Raman spectra have measurable chirality dependence. This was possible by placing camphor on a symmetry-matching substrate of SiO_2 and enforcing molecular orientation. These states can be called enantiomeric, as they exhibited clear differences between camphor enantiomers by the noncoincidence effect, depolarization ratio, and molecular orientation. The occupancy ratio of these vibronic states separated by $\sim 1.8 \text{ cm}^{-1}$ was four times larger in one enantiomer compared to the other, as expected. This simple, but powerful, method can be applied for chirality detection and quantification of chiral molecules.

Main Text

Introduction

The Jahn-Teller (JT) effect, symmetry breaking of nonlinear nuclear configurations through vibronic coupling with degenerate electronic states (DES) in molecules (1), has led to great breakthrough in molecular science and engineering (2). One immediate consequence of the JT effect, the pseudo-JT (PJT) effect (3), can be the reason of sub-meV split excited-DES that can be used to discriminate enantiomers (4). Few decades ago, it was found that the vibrational Raman optical activity (ROA) can be used to determine conformation in chiral molecules. In the exemplar chiral molecule of camphor ($C_{10}H_{16}O$), the Raman circular intensity differential, in which small difference in the intensity of vibrational Raman scattering of right- and left-circularly polarized incident light can be detected (5), was used for various chiral camphor dissolved in solvents like carbon disulfide. They exhibited degenerate vibrational states (so-called couplets) with strong intensity around 500 cm^{-1} , which were assigned to the in- and out-of-plane deformation modes of carbonyl ($C=O$) group of camphor (5). Subsequent calculations (6) in 3-methylcyclohexanone, which has $C=O$, ring, and methyl groups as in camphor, showed that 3C deformation, either in ring or ring-methyl group, could also be the reason behind these couplets in ROA, as well as in-plane $C=O$ deformation, based on bond polarizability (7). Despite it can provide direct discrimination of molecular chirality, ROA signals are weaker in intensity compared to Raman signals due to the measurement technique. Besides, inevitable solvation effects (8) adds more complexity in elucidation of the degenerate vibrational states in camphor.

When the Raman processes are resonant, there will be vibronic interactions. Then, one has to consider the degeneracy of electronic states rather than vibrational states, since the polarizability depends on vibrational perturbation of electronic states that accounts for sum over all excited states (Albrecht's approach) (9). A direct consequence of the latter is the Herzberg-Teller vibronic coupling, which was conveniently utilized in explanation of

surface enhanced Raman scattering of molecules on metal substrates (10). For chiral molecules, the interactions between molecules and modified surfaces can trigger amplification of chirality by asymmetry induction (11) and chiral information transfer (12). However, these wouldn't be feasible for metal containing surfaces due to pure plasmonic and photothermal effects. This emphasizes the role of dielectric substrates, which can assist in focusing the electric field (E -field) lines (from far to near) for signal enhancement (13). In a recent work, a substrate consisting of silicon nanodisk array with C_4 symmetry (providing isotropic response to the incident light) was employed for optical chirality enhancement in the case of α -pinene and tartaric acid (14).

Here, we report that symmetry reduction with respect to chiral centers (15) of an exemplar chiral molecule of camphor can lead to chiral discrimination and quantification. By resonance Raman scattering (RRS), the chirality-dependent vibronic degenerate modes can be accessed in chiral camphor, with D_{6h} symmetry of its carbon-ring being reduced to chiral C_3 , after being placed on silicon dioxide (SiO_2)/Si substrate.

Results

Enantioselective E-field-driven RRS in a PJT system A practical model of vibronic coupling by RRS in chiral camphor, based on an existing theory (16), is depicted in Fig. 1, for ring or ring-methyl part of camphor. Light (with 2.33 eV photon energy) linearly polarized in the x -direction is incident (with intensity I_{ix}) normal to the surface where camphor (either right-chiral D or left-chiral L camphor) is placed on a SiO_2 substrate; and the light scattering can be back in the x - or z -direction, with intensities I_{sx} (polarized) and I_{sz} (depolarized), respectively (left side of Fig. 1A). The initial light polarization angle at normal incidence is ϕ (fixed at 0°) on the SiO_2 /Si substrate; while the relative angle β is the scattering polarization angle that is defined with respect to ϕ (right side of Fig. 1A). Upon light absorption, transitions take place from nondegenerate ground electronic state $^1A_{1g}$ to the excited doubly-degenerate electronic (Q-band) states $^1B_{2g}$ via e -type vibrational mode, e_{1g} and b_{2g} , involving six-carbon ring of camphor, as shown in Fig. 1B. The Raman

processes are between the vibrational modes in $^1B_{2g}$, which can be understood in terms of the Herzberg-Teller vibronic coupling (17), or $(^1A_{1g} + ^1B_{2g}) \otimes e$ pseudo-Jahn-Teller (PJT) effect (3, 18). A simplified schematic of adiabatic potential energy surface in the aforementioned PJT effect is presented in Fig. 2A, in which the symmetry reduces from D_{6h} to D_{3h} , where both of two chiral centers (identified by dark green and dark orange colors in Fig. 2B) in camphor form their own C_3 point group with two light green and light orange colors, respectively (shown in Fig. 2C). This non-centrosymmetric trigonal point group is known to have chirality dependence (19) and it can be a determining factor and possibly a difference in response to an external field, for camphor enantiomers.

The ground state in Fig. 2A is the nondegenerate (originally stable) A_1 state; however, the strong PJT coupling between the excited states E_2 and E_1 enforces a JT distortion at a distance q_0 from the carbon-ring center and causes an additional global minimum, which underlines a coexisting C_{2v} symmetry (Fig. 2B). In this picture, E_2 and E_1 are low-lying excited-DES, and only possible source of symmetry breaking and degeneracy is the PJT interaction. Paying a close attention to the case of no distortion, one can see that E_2 and E_1 have similar feature at the center as expected by generalized maximum hardness principle (GMHP) for excited states, meaning softer and more polarizable with respect to the ground state (20), while there is an asymmetry at nuclear displacement indicating non-totally symmetric vibration mode becoming active by the PJT effect between E_2 and A_1 (both have the same low symmetry) (21). This exception to the GMHP, together with minimum polarizability expectation at excited states (22), becomes more meaningful for a dissymmetric medium consisting of camphor on SiO_2/Si substrate, as there is a low symmetry match between carbon ring of camphor and SiO_2 . Here, we need to remember that the chirality of refracted light field (simply “ E -field” as no magnetism is involved) in this medium will be inversion symmetric and time reversal (TR) invariant (23), and the polarization state of the light (represented by polarization vector $\mathbf{e} = (1, i, 0)/\sqrt{2}$ in a basis where the wave vector \mathbf{k} is parallel to the z -axis) can turn into an elliptical one. It was recently shown that even the chirality of circularly polarized light could be enhanced in systems consisting of dielectric substrates and chiral molecules (24). For our dissymmetric

medium, the E -field–polarization vector interaction (\mathbf{Q}) can be thought as two-photon interaction ($(\mathbf{e} \mathbf{k}) \rightleftharpoons (\mathbf{e}' \mathbf{k}')$), during which the linearly polarized light can be turned into circularly polarized light, then back to linearly polarized state (25). In the case of RRS, this would correspond to electric Raman linear dichroism, where \mathbf{Q} has the form $e(\mathbf{e}^* \times \mathbf{E})$ given the material has C_3 symmetry in an oriented system (19, 25). Therefore, the only source of spontaneous breaking of inversion symmetry should be due to the interaction between the E -field and a molecule with specific chirality (19, 25–26). Then, our physical system of chiral camphor– E -field can be simply described as a density matrix of (27).

$$\begin{pmatrix} \rho_{11} & (\zeta) \rho_{12} \\ (\zeta^*) \rho_{21} & \rho_{22} \end{pmatrix}$$

Here, diagonal elements ρ_{11} and ρ_{22} are purely about camphor vibronic states either $\varphi_R(A_{10}, E_{10}, E_{20})$ or $\varphi_L(A_{10}, E_{10}, E_{20})$, for right and left molecular chirality, respectively (and resulting in most probable density of states, or occupancy η , for each case); while the off-diagonal elements $(\zeta)\rho_{12}$ and $(\zeta^*)\rho_{21}$ are camphor– E -field interaction terms, where $\zeta = \zeta$ ($\varphi_{//}^P, \varphi_{\perp}^P$), and $\varphi_{//}^P$ and φ_{\perp}^P are the orthogonal (probing) light polarization states, for polarized and depolarized cases, respectively. Finally, the enantioselective E -field-driven RRS, which has yielded $//$ (\perp) contribution upon $//$ incident polarization, from our dissymmetric system consisting of either D or L camphor with C_3 symmetry on SiO_2 substrate, as shown in Fig. 2C, can distinguish between enantiomers in the basis of the vibronic states with energies E_2 and E_1 , as depicted in Fig. 2D (Fig. 2E). This is mainly due to the two vibronic couplings E_2 – E_1 and E_2 – A_1 , which further results in depolarization ratio $R_i = E_{i\perp} / E_{i//}$, for $i = (1, 2)$, that would differ for camphor enantiomers (Fig. 2E).

Raman spectra and PJT states in chiral camphor Unpolarized RRS of camphor is quite similar to a previous report on solid D camphor (28). Spectra for D and L camphor are given in Fig. 3A and Fig. 3B, respectively. The observed relatively large peak at 652 cm^{-1} is due to six-carbon ring vibration and a clear peak at 1740 cm^{-1} is due to the C=O stretching. The remaining peak assignments can be made as follows: 1474 cm^{-1} CH_3 asymmetric deformation (29), 912, 987, and 1016 cm^{-1} methyl rocking (5), 857, 1097, 1416, and 1447 cm^{-1} due to various ring and C–H modes (28). Besides, the peak at 950 cm^{-1}

¹ is known as symmetric stretching vibrations of tetrahedral silicate (SiO₂ substrate), sensitive to molecules (30); while peaks in the 430-600 cm⁻¹ region are mixed with Si-O-Si bending (31) and stretching modes, as well as Si LO mode (*SI Appendix*, Fig. S1). Although SiO₂ is amorphous, there are features of α -quartz and local D_3 symmetry (32) (*SI Appendix*, note 1). Also, the anisotropy of short-range forces and splitting introduced by the crystal field can be prominent (33).

In our polarization-dependent Raman measurements, spectra of camphor on SiO₂/Si substrate showed a clear variation from SiO₂/Si substrate alone, and a slight variation in peak position of Si 520 cm⁻¹ between the cases of camphor enantiomers on SiO₂/Si substrate, which can be explained by optical dissymmetry (24) (*SI Appendix*, Fig. S2-S3 and note 1). On the other hand, all the peaks, including methyl-related ones, in the Raman spectra of Fig. 3A and B, exhibited a qualitatively similar polarization dependence for both camphor (*SI Appendix*, Fig. S4 and note 2), except the peaks at 652 cm⁻¹, for which the insets indicate an asymmetric band for both camphor and a distinction between two camphor. By higher resolution measurements in the 620-680 cm⁻¹ region, polarized (depolarized) RRS of two camphor are compared in Fig. 3C and D (Fig. 3E and F). For polarized RRS, two peaks around 649 cm⁻¹ separated by approximately 1.8 cm⁻¹ are eminent, in addition to a separate peak around 666 cm⁻¹. By fitting Lorentzian functions, the peak positions (or energies) are determined for both camphor (Table 1) for the energies associated with excited states E_2 , E_1 , and the ground state A_1 , respectively. Here, E_2 and E_1 are the PJT states. The peak intensities for A_1 and E_1 are about the same, which is a consequence of the aforementioned PJT effect between these similar low symmetry states (20) and the expectation of invariance in potentials and coupling with E_1 for the non-totally symmetric mode A_1 (34); while E_2 is relatively larger than its counterpart E_1 , as a result of the harmonicity, the strong PJT effect between the E_2 - E_1 doublet, and the small energy gap between these states leading to an asymmetric distortion (35). The difference in intensity between E_2 and E_1 vibronic states could be partly reminiscent of degenerate vibrational states due to C=O deformation (5), which could be mixed with ring or ring-methyl group in this case (7). The full-width half-maximum (FWHM) of the peaks associated with E_2 ,

E_1 , and A_1 shown in Table 1 are qualitatively in agreement with the expectation from a tight-binding model for six-carbon ring geometry (36), several times smaller than the bandwidth of C_{60} (37). Most noticeable feature of the polarized RRS in Fig. 3C and D is the narrowing of all the bands for L camphor compared to those of D camphor, while peak intensities didn't exhibit much variation.

Discussion

Chiral discrimination by PJT states, depolarization, and noncoincidence effect The depolarized spectra in Fig. 3E and F exhibit clear differences. The peak energies associated with E_2 , E_1 , and A_1 are tabulated in Table 1. Apparently, in the depolarized RRS there are 3.2 and 2 cm^{-1} separation between two camphor, for peak energies associated with the PJT states E_2 and E_1 , respectively, (negligible difference for A_1) which cannot be observed in the polarized spectra. Polarization relative angle β dependence of all the peak energies for both camphor are compared in Fig. 4A and B. When $\beta = \pm 90^\circ$ (depolarized), in the case of L camphor, a redshift (from the polarized spectra) of 2.5 and 1.5 cm^{-1} in E_2 and E_1 , respectively, is noticeable, and a slight blueshift can be argued in both E_2 and E_1 for D camphor (Fig. 4A); while there is only small ($\sim 0.5 \text{ cm}^{-1}$) random fluctuation in A_1 for both camphor (Fig. 4B). The frequency shifts can be understood as a difference between the isotropic and anisotropic Raman spectra, which has been observed in molecular liquids, accepted as manifestation of the intermolecular coupling (38) and the Raman noncoincidence effect (NCE) (39). In the depolarized spectra of Fig. 3E and F, the FWHM of the peaks associated with E_2 , E_1 , and A_1 are shown in Table 1. Although the more (less) dominant NCE observed in L camphor (D camphor) indicates large (small) variation between isotropic and anisotropic parts of totally symmetric portion of vibrational mode (38), the relatively larger (smaller) enhancements of linewidths suggest relatively weaker (stronger) anisotropic behavior, most likely (not) influenced by the orientation of C=O part of the six-carbon ring on the SiO_2 substrate (environment effect) (40).

The depolarization ratio $R = I_{\perp} / I_{\parallel}$ for peak intensities associated with E_2 , E_1 , and A_1 can be extracted from Fig. 3C to F, as 14.1 (6.0), 6.6 (9.4), and 13.1 (10.3) % for D camphor (L camphor), respectively. These R values can be compared with the calculated values of transition polarizability tensor α in the molecular frame, in which the scattering Raman signal is the average over all molecular orientations (41). For an asymmetric six-carbon ring-based structure, there are three invariants consisting of α elements: symmetric isotropic, anti-symmetric anisotropic, and symmetric anisotropic. Assuming the anisotropy is only in the x-direction, there would be two possible calculated R values for two different excited vibrational modes, 6.9 or 11.5 % (SI Appendix note 3). This supports the observation of higher (lower) R in D camphor and lower (higher) R in L camphor for E_2 (E_1); while R for A_1 follows whichever excited vibrational mode is persistent against rotation. Fig. 4C and D suggest that molecular polarizability is shifted about ~ 15 (8) $^{\circ}$ for D camphor (L camphor) which occurs as deviation from its expected minimum at the depolarization, especially more evident for the peak associated with E_2 . This can be considered as a consequence of the chiral molecule- E -field (excitation) interaction and non-totally symmetric scattering. This is an expected outcome of a forced orientation similar to the observation in di-D-phenylalanine molecules in a nanotube geometry (42).

Chirality dependence of PJT states occupancy ratio Peak energies, intensities, and bandwidths have evidenced possibility of chirality-dependent NCE, depolarization ratio, and molecular orientation via PJT states, rather approximately. Furthermore, it is feasible to obtain estimates of occupancy, η , of these states, by using the same RRS data, through integrating areas under peaks associated with E_2 and E_1 . This can allow to analyze vibronic density of states within the frame of chiral molecule- E -field interaction. The polarization relative angle β dependence of the integrated intensities for peaks associated with E_2 , E_1 , and A_1 are plotted in Fig. 4E and F, for D and L camphor, respectively, which follow the peak intensity profile in Fig. 4C and D, except that the occupancy probabilities of E_1 are clearly smaller than those of E_2 and A_1 . Unlike the polarization dependence of peak intensities (in which E_1 and A_1 exhibit more similar behavior), the trends of E_2 and A_1 are more alike in polarization dependence of integrated areas, evidencing several underlying

physical mechanisms. Firstly, this indicates there is mixed vibrational and electronic transitions. The polarization characteristics of both the vibrational (which can be defined by peak intensities) and the vibronic (defined by integrated intensities) components can be differentiated. Also, there could be two specific states-mixing scenarios: the first one is the mixing of one vibrational level of one excited-DES (such as E_2) and other vibrational level of the other excited-DES (such as E_1) (26), and the second one is the mixing of PJT states (split by only 1.8 cm^{-1} or 0.18 meV) in the context of enantiomeric interconversion at room temperature, such as in helicene (28). The latter scenario could be the reason behind the quite similar behavior between enantiomers away from depolarization that can be seen in Fig. 4E and F.

The occupancy η of the vibronic states (or excited-DES, $\eta(E_2)$ and $\eta(E_1)$, which are directly proportional to the integrated intensities) reflect the most probable density of states for each case. This can allow us to define a state polarization.

$$P = \frac{\eta(E_2) - \eta(E_1)}{\eta(E_2) + \eta(E_1)}$$

Polarization relative angle β dependence of P are compared in Fig. 4G. There is no clear distinction between two camphor from polarized state (0°) to $\pm 70^\circ$, and P varies between 0-70 (15-70) % for D camphor (L camphor). However, a discrimination between enantiomers can be seen at large angle of β : P stays at high (low) values above (below) 75 % between $\pm 70^\circ$ and depolarized state ($\pm 90^\circ$). The occupancy ratio, $\eta(E_2)/\eta(E_1)$, in Fig. 4H can describe the molecular chirality dependence, which is ~ 8 and ~ 2 for D and L camphor in the depolarized state and varies between 2 and 4 for β between 0 and $\pm 70^\circ$. Here, we need to remind that this observation was only possible as a result of the chirality-dependence of these PJT states at the depolarized Raman. At the polarized Raman, the polarization P is ~ 50 %, corresponding to an occupancy ratio of ~ 3 , for both camphor; these values increase (decrease) to ~ 75 (25) % and 8 (2), respectively, for D camphor (L camphor) at the depolarized Raman, which reveals the molecular chirality-dependent pseudo-Jahn-Teller states. The data presented in Figs. 3 and 4 are taken on one spot on the

sample; thanks to homogeneity, results were qualitatively similar for other samples and spots ([Materials and Methods](#), [SI Appendix Fig. S5](#)).

The change in linewidths of the excited vibronic states from the polarized state to the depolarized state in D camphor is weaker ($\sim +25\%$) than L camphor ($\sim +75\%$). This is attributed to nonlinear effects, such as optical rotation ([43](#)), which has molecular chirality dependence for C_3 systems ([44](#)). For non-rotating chiral molecules, enantiomeric states should obey the Hund's rule ([45](#)) and time-odd polarizability applies. Therefore, it is conceivable the optical rotation is opposite for odd-electron molecules, with opposite chirality ([46](#)).

Materials and Methods

Sample preparation Four-inch wafers of SiO_2 (300 nm thick) on silicon (100) single-crystal (SiO_2/Si) were used as substrate. Camphor enantiomers were purchased from Acros Organics™ (now known as Thermo Scientific™): (1R)-(+)-camphor (or D camphor) and (1S)-(-)-camphor (or L camphor), both 98 %. Sample preparation was as follows. After being sliced to pieces of 1 cm x 1 cm, the SiO_2/Si substrates were cleaned with a usual cleaning process of acetone, isopropyl alcohol, and DI water for 5 min each in ultrasonic cleaner. The solution was prepared in a clean room environment, just before measurements, at temperature of $20 \pm 2\text{ }^\circ\text{C}$. According to the standards, at $25\text{ }^\circ\text{C}$, a solution of camphor with chloroform requires 1 g of camphor and 0.5 mL of chloroform, which made the evaporation process relatively slower at a temperature of $20 \pm 2\text{ }^\circ\text{C}$. For the purpose of uniform thickness of camphor film on SiO_2/Si substrate, 1/9 g of camphor was used in 0.5 ml of chloroform, which is a recipe found to be the optimum condition to get a reasonable and reproducible Raman signal. The prepared solution was stirred for 15 min at ambient conditions to make the solution more homogeneous; then dropped onto a SiO_2/Si substrate, with each drop amount of 0.5 μL , by using 0.1 - 2.5 μL pipette.

Micro-Raman measurements A Witech brand micro-Raman system with 520 nm excitation and laser power of ~ 5 mW was used. A neutral density filter was placed between the source and the polarizer unit to prevent the over exposure; and the reason of choice of power was to avoid the heating of the samples. A $100\times$ microscopic lens (0.6 N.A.) was used for focusing the light beam on the sample, which made the spatial resolution about 1 μm , and the spectrum resolution was a little less than 0.5 cm^{-1} . Polarized Raman measurements were performed by two rotatable half-wave plates as converging the incident beam on the sample and collecting the scattered light from the sample in the z-direction (as in Fig. 1A). The polarization of the incident light was kept the same by fixing the first half-wave plate to 0° . For the scattered light, the polarizer (or the analyzer in this case) was used, and the polarization direction of the light that enters the spectrometer was perpendicular to the groove direction of the grid, which was set as to 0° of the second half-wave plate. This was done to ensure that the polarization dependencies of grating will not affect the results. In the data analysis, the polarization dependencies of the beam transmission rate were measured and compensated. Polarization dependent measurements were performed by varying the analyzer half-wave plate 10° from -90° to 90° for the specific region of six-carbon ring (between $630\text{--}680\text{ cm}^{-1}$ with 0.5 cm^{-1} data step size). All the data sets are the averaged spectra over 20 scans, for each camphor, (0° and 90° data for both camphor are presented in Fig. 3C to F) which were finally fit to three Lorentzian and obtained fitting parameters were plotted in Fig. 4A to F.

Acknowledgments

We thank Xiaochun Hang (NanjingTech) for fruitful discussions on chirality and symmetry in chemistry. Funding sources are as follows: National Natural Science Foundation of China grant NSFC 11774170 (ME); 100 Foreign Talents Project in Jiangsu Province grant JSA2016003 (ME); National Natural Science Foundation of China grant NSFC 51772145 (YH); National Natural Science Foundation of China grant NSFC 62288102 (WH); National Key Research and Development Program of China grant 2020YFA0709900 (WH).

References

1. H. A. Jahn, E. Teller, Stability of Polyatomic Molecules in Degenerate Electronic States. I. Orbital Degeneracy. *Proc. R. Soc. Lond. A*, **161**, 220–235 (1937). doi:10.1098/rspa.1937.0142
2. A. Ceulemans, *The Theory of the Jahn–Teller effect: When a Boson Meets a Fermion* (Springer, New York, 2022). doi:10.1007/978-3-031-09528-3
3. I. B. Bersuker, Pseudo-Jahn-Teller Effect—a Two-State Paradigm in Formation, Deformation, and Transformation of Molecular Systems and Solids. *Chem. Rev.* **113**, 1351–1390 (2013). doi:10.1021/cr300279n
4. Y.-N. Chiu, Opto-Vibronic Generation of Chirality via Jahn-Teller Distortion of Odd- and Even-Spin Molecules. *J. Phys. Chem.* **88**, 5820–5826 (1984). doi:10.1021/j150668a016
5. L. D. Barron, Raman Optical Activity of Camphor and Related Molecules. *J. Chem. Soc., Perkin Trans.* **2**, 1074–1079 (1977). doi:10.1039/P29770001074
6. P. L. Polavarapu, L. A. Nafie, Vibrational Optical Activity: Comparison of Theoretical and Experimental Results for (+)-(3R)-Methylcyclohexanone. *J. Chem. Phys.* **73**, 1567–1575 (1980). doi:10.1063/1.440336
7. L. D. Baron, J. F. Torrance, J. Vrbancich, Raman Optical Activity in Carbonyl Deformations. *J. of Raman Spectrosc.* **13**, 171–177 (1982). doi:10.1002/jrs.1250130213
8. P. Lahiri, K. B. Wiberg, P. H. Vaccaro, Intrinsic Optical Activity and Conformational Flexibility: The Role of Size-Dependent Ring Morphology in Model Cycloketones. *J. Phys. Chem. A*, **117**, 12382–12400 (2013). doi:10.1021/jp4089194
9. C. A. Albrecht, On the Theory of Raman Intensities, *J. Chem. Phys.* **34**, 1476–1484 (1961). doi:10.1063/1.1701032
10. J. R. Lombardi, R. L. Birke, A Unified Approach to Surface-Enhanced Raman Spectroscopy. *J. Phys. Chem. C*, **112**, 5605–5617 (2008). doi:10.1021/jp800167v

11. M. Das, D. Gangopadhyay, J. Šebestík, L. Habartová, P. Michal, Josef Kapitán, Petr Bouř, Chiral Detection by Induced Surface-Enhanced Raman Optical Activity. *Chem. Commun.* **57**, 6388–6391 (2021). doi:10.1039/D1CC01504D
12. S. Ostovarpour, L. Rocks, K. Faulds, D. Graham, V. Parchaňský, Petr Bouř, Ewan W. Blanch, Through-Space Transfer of Chiral Information Mediated by a Plasmonic Nanomaterial. *Nat. Chem.* **7**, 591–596 (2015). doi:10.1038/nchem.2280
13. O. J. Glembocki, R. W. Rendell, D. A. Alexson, S. M. Prokes, A. Fu, M. A. Mastro, Dielectric-Substrate-Induced Surface-Enhanced Raman Scattering. *Phys Rev. B*, **80**, 085416 (2009). doi:10.1103/PhysRevB.80.085416
14. T.-H. Xiao, Z. Cheng, Z. Luo, A. Isozaki, K. Hiramatsu, T. Itoh, M. Nomura, S. Iwamoto, K. Goda, All-Dielectric Chiral-Field-Enhanced Raman Optical Activity. *Nat. Commun.* **12**, 3062 (2021). doi:10.1038/s41467-021-23364-w
15. R. S. Cahn, Sir C. Ingold, V. Prelog, Specification of Molecular Chirality. *Angew. Chem. Internat. Edit.* **5**, 385–415 (1966). doi:10.1002/anie.196603851
16. M. Z. Zgierski, M. Pawlikowski, Theory of Resonance Raman Scattering by Doubly Degenerate Modes. *J. Chem. Phys.* **71**, 2025–2043 (1979). doi:10.1063/1.438594
17. Y. Nishimura, A. Y. Hirakawa, M. Tsuboi, A Vibronic Coupling in a Degenerate Electronic State via a Nuclear Momentum and an Antisymmetric Raman Scattering Tensor. *J. Chem. Phys.* **67**, 1009–1014 (1977). doi:10.1063/1.434977
18. A. R. Ilkhani, Pseudo Jahn-Teller Origin of Puckering in Cyclohexahomoatomic Molecules E₆ (E = S, Se, Te) and Restoring S₆ Planar Ring Configuration. *J. Mol. Struct.* **1098**, 21–25 (2015). doi:10.1016/j.molstruc.2015.05.029
19. J. Kishine, H. Kusunose, H. M. Yamamoto, On the Definition of Chirality and Enantioselective Fields. *Isr. J. Chem.* **62**, e202200049 (2022). doi:10.1002/ijch.202200049
20. W. Grochala, The Generalized Maximum Hardness Principle Revisited and Applied to Atoms and Molecules. *Phys. Chem. Chem. Phys.* **19**, 30964–30983 (2017). doi:10.1039/C7CP03101G
21. L. Blancafort, M. Torrent-Sucarrat, J. M. Luis, M. Duran, Miquel Solà, Evaluation of the Analogy between Exceptions to the Generalized Maximum Hardness Principle for

- Non-Totally-Symmetric Vibrations and the Pseudo-Jahn-Teller Effect. *J. Phys. Chem. A*, **107**, 7337–7339 (2003). doi:10.1021/jp034557n
22. M. Torrent-Sucarrat, J. M. Luis, M. Duran, M. Solà, On the Validity of the Maximum Hardness and Minimum Polarizability Principles for Nontotally Symmetric Vibrations. *J. Am. Chem. Soc.* **123**, 7951–7952 (2001). doi:10.1021/ja015737i
23. L. D. Barron, Parity and Optical Activity. *Nature*, **238**, 17–19 (1972). doi:10.1038/238017a0
24. Y. Tang, A. E. Cohen, Enhanced Enantioselectivity in Excitation of Chiral Molecules by Superchiral Light. *Science*, **332**, 333–336 (2011). doi:10.1126/science.120281
25. G. E. Stedman, Polarization Dependence of Natural and Field-Induced One-Photon and Multiphoton Interactions. *Adv. Phys.* **34**, 513–587 (1985). doi:10.1080/00018738500101811
26. L. D. Barron, Symmetry and Chirality: Where Physics Shakes Hands with Chemistry and Biology. *Isr. J. Chem.* **61**, 517–529 (2021). doi: 10.1002/ijch.202100044
27. M. Simonius, Spontaneous Symmetry Breaking and Blocking of Metastable States. *Phys. Rev. Lett.* **40**, 980–983 (1978). doi:10.1103/PhysRevLett.40.980
28. S. Sharma, G. Kalita, M. E. Ayhan, K. Wakita, M. Umeno, M. Tanemura, Synthesis of Hexagonal Graphene on Polycrystalline Cu Foil from Solid Camphor by Atmospheric Pressure Chemical Vapor Deposition. *J. Mater. Sci.* **48**, 7036–7041 (2013). doi:10.1007/s10853-013-7514-3
29. S. Senthilkumar, M. Briget Mary, and V. Ramakrishnan, Infrared and Raman Spectroscopic Studies of L-valinium Picrate. *J. of Raman Spectrosc.* **38**, 288–294 (2007). doi:10.1002/jrs.1641
30. P. G. Pai, S. S. Chao, Y. Takagi, G. Lucovsky, Infrared Spectroscopic Study of SiO_x Films Produced by Plasma Enhanced Chemical Vapor Deposition. *J. Vac. Sci. Technol. A*, **4**, 689–694 (1986). doi:10.1116/1.573833
31. H. Liu, H. Kaya, Y.-T. Lin, A. Ogrinc, S. H. Kim, Vibrational Spectroscopy Analysis of Silica and Silicate Glass Networks. *J. Am. Ceram. Soc.* **105**, 2355–2384 (2022). doi:10.1111/jace.18206

32. M. K. Gunde, Vibrational Modes in Amorphous Silicon Dioxide. *Physica B*, **292**, 286–295 (2000). doi:10.1016/S0921-4526(00)00475-0
33. J. F. Scott, S. P. S. Porto, Longitudinal and Transverse Optical Lattice Vibrations in Quartz. *Phys. Rev.* **161**, 903–910 (1967). doi:10.1103/PhysRev.161.903
34. W. H. Henneker, A. P. Penner, W. Siebrand, M. Z. Zgierski, Anharmonic Potentials and Vibronic Energy Levels for Closely Coupled Molecular Electronic States. *Chem. Phys. Lett.* **45**, 407–410 (1977). doi:10.1016/0009-2614(77)80049-3
35. W. H. Henneker, A. P. Penner, W. Siebrand, M. Z. Zgierski, Resonance Raman Scattering in Molecules with Double Minimum Potentials. *Chem. Phys. Lett.* **48**, 197–200 (1977). doi:10.1016/0009-2614(77)80299-6
36. C. H. Xu, C. Z. Wang, C. T. Chan, K. M. Ho, A Transferable Tight-Binding Potential for Carbon. *J. Phys.: Condens. Matter.* **4**, 6047–6054 (1992). doi:10.1088/0953-8984/4/28/006
37. J. Yu, R. K. Kalia, P. Vashishta, Effect of Pressure on Intermolecular and Intramolecular Phonons in Solid C₆₀. *J. Chem. Phys.* **99**, 10001–10010 (1993). doi:10.1063/1.465504
38. M. G. Giorgini, Raman Noncoincidence Effect: A Spectroscopic Manifestation of the Intermolecular Vibrational Coupling in Dipolar Molecular Liquids. *Pure Appl. Chem.* **76**, 157–169 (2004). doi:10.1351/pac200476010157
39. G. Fini, P. Mirone, Evidence for Short-Range Orientation Effects in Dipolar Aprotic Liquids from Vibrational Spectroscopy Part 2.–Carbonyl Compounds. *J. Chem. Soc., Faraday Trans. 2*, **70**, 1776–1782 (1974). doi:10.1039/F29747001776
40. H. Wang, H. Xu, Q. Liu, X. Zheng, The Noncoincidence Phenomenon of Acetonylacetone C=O Stretching in a Binary Mixture and the Aggregation-Induced Split Theory. *RSC Adv.* **10**, 30982–30989 (2020). doi:10.1039/F29747001776
41. C. Sourisseau, Polarization Measurements in Macro- and Micro-Raman Spectroscopies: Molecular Orientations in Thin Films and Azo-Dye Containing Polymer Systems. *Chem. Rev.* **104**, 3851–3891 (2004). doi:10.1039/D0RA02932G
42. V. Sereda, N. M. Ralbovsky, M. C. Vasudev, R. R. Naik, I. K. Lednev, Polarized Raman Spectroscopy for Determining the Orientation of di-D-phenylalanine

- Molecules in a Nanotube. *J. of Raman Spectrosc.* **47**, 1056–1062 (2016).
doi:10.1002/jrs.4884
43. P. Fischer, F. Hache, Nonlinear Optical Spectroscopy of Chiral Molecules. *Chirality*, **17**, 421–437 (2005). doi:10.1002/chir.20179
44. Y.-N. Chiu, Degenerate States in Optical Rotation and Time-Reversal Invariances. *Phys. Rev. A*, **32**, 2257–2269 (1985). doi:10.1103/PhysRevA.32.2257
45. L. Rosenfeld, Quantenmechanische Theorie der Natürlichen Optischen Aktivität von Flüssigkeiten und Gasen. *Z. Phys.* **52**, 161–174 (1929). doi:10.1007/BF01342393
46. Y.-N. Chiu, Optical Rotation of Time-Reversal Degenerate States. *Jnl. Chinese Chemical Soc.* **32**, 201–206 (1985). doi:10.1002/jccs.198500033

Figure 1

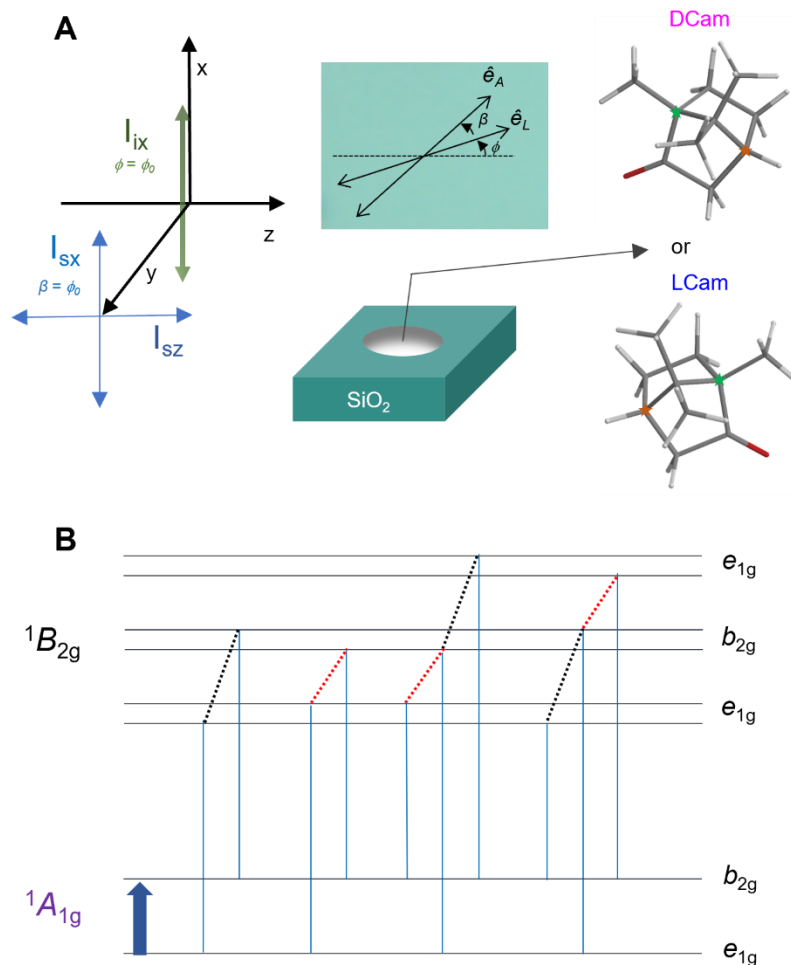


Fig. 1. Linearly polarized Raman spectroscopy and Raman transitions of camphor molecules on SiO_2/Si substrate. (A) Linearly polarized light incident in the x-direction with intensity I_{ix} (normal to the surface of camphor, along the unit vector \hat{e}_L , either right-chiral D or left-chiral L camphor, on a SiO_2/Si substrate) and the scattered light in the x- or z-direction, with intensities I_{sx} (polarized) and I_{sz} (depolarized), respectively (along the unit vector \hat{e}_A). The initial light polarization angle at normal incidence is ϕ (fixed at 0°); while the relative angle β is the scattering polarization angle can vary with respect to ϕ . Two stars (colored differently, orange and green) on the D and L camphor represent the chiral centers (B) Raman transition from nondegenerate ground electronic state $^1A_{1g}$ to excited doubly-degenerate electronic (Q-band) states $^1B_{2g}$ via e-type vibrational mode, e_{1g} and b_{2g} , involving six-carbon ring of camphor.

Figure 2

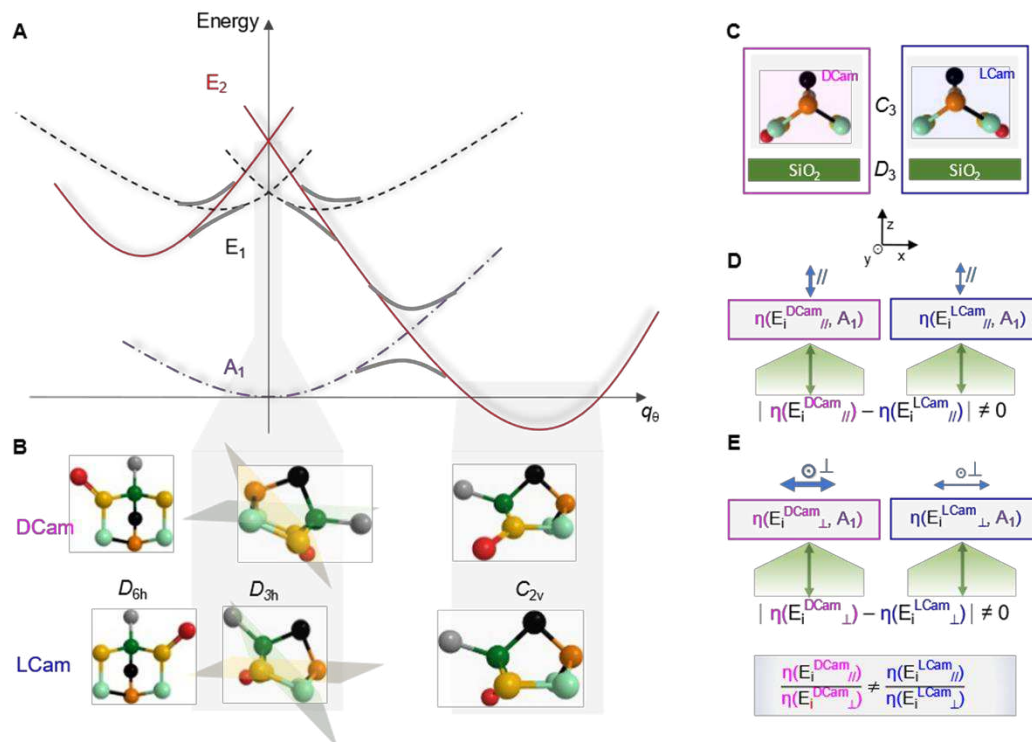


Fig. 2. Vibronic model for chiral camphor on SiO₂. (A) Schematic of adiabatic potential energy surface for six-carbon ring of camphor with D_{6h} symmetry, with (¹A_{1g} + ¹B_{2g}) ⊗ e pseudo-Jahn-Teller (PJT) coupling, which are the solid connecting lines, the nondegenerate ground state A₁ (dash-dot line), the excited states E₂ (dot line) and E₁ (dash line) are shown (not to scale) (B) Symmetry reduction from D_{6h} to D_{3h} by the PJT between the E₂ and E₁; also, a JT distortion at a distance q₀ from the carbon-ring center leading to a coexisting C_{2v} symmetry. Color coding: one dark and two orange (green) C atoms form C₃ symmetry (C) Placing camphor on SiO₂ substrate and C₃ symmetry becoming intact. Occupancy η of camphor vibronic states (A₁ and E_i, where i = 1 or 2) in polarized (D) and depolarized (E) Raman spectrum, respectively; an imbalance of occupancy ratio of the excited states.

Figure 3

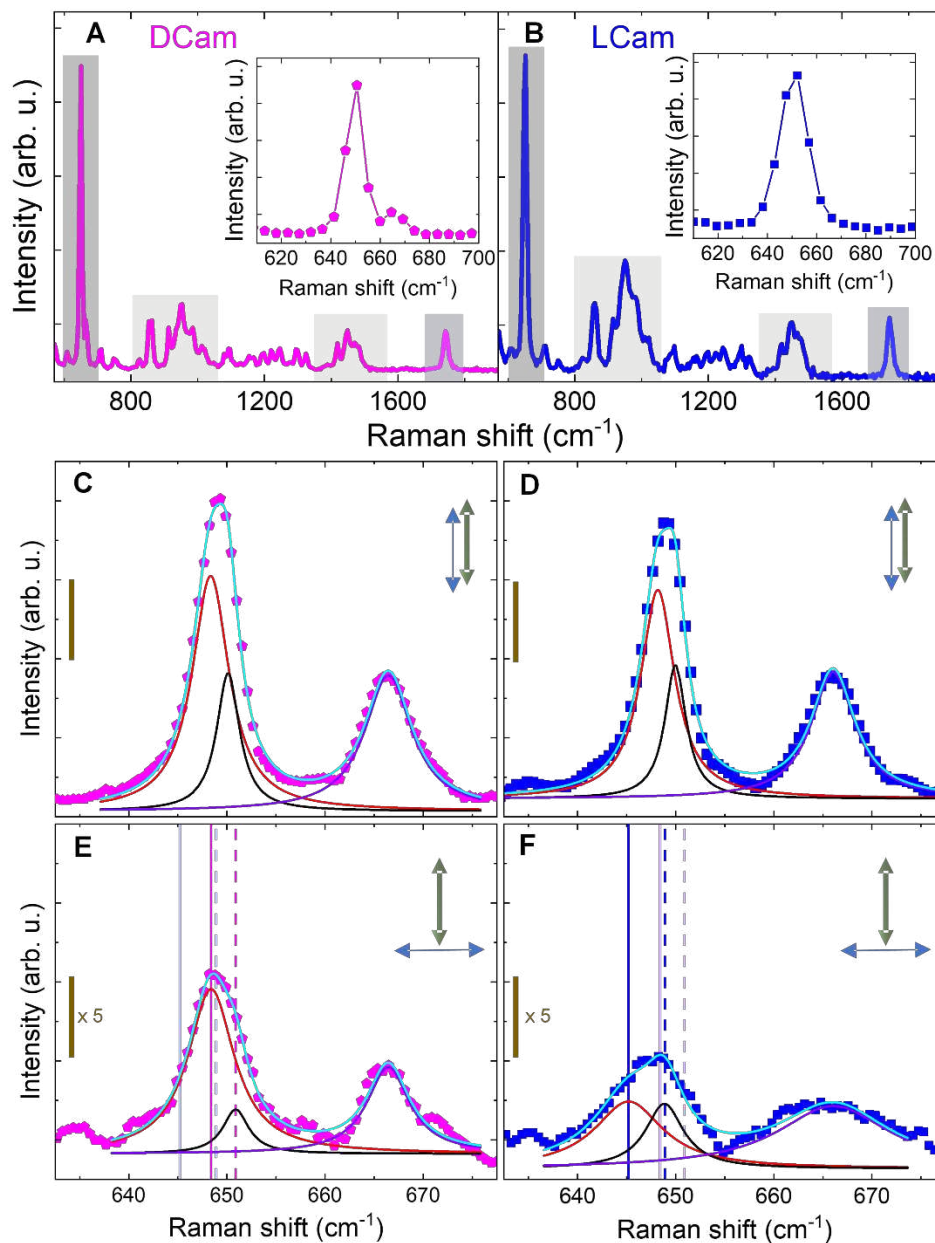


Fig. 3. Unpolarized, polarized, and depolarized Raman spectra of camphor enantiomers. Unpolarized Raman spectra for D camphor (A) and L camphor (B), respectively. Peak around 652 cm⁻¹ assigned to the six-carbon ring (zoomed in insets), other peaks assignments are given in the text. (C)-(D) show polarized Raman for D camphor and L camphor, respectively; data fitted to three Lorentzian functions associated with E₂, E₁, (splitting of these PJT states is ~ 1.8 cm⁻¹) and A₁ with increasing wave number (red, black,

and violet). Similarly, (E)-(F) show depolarized Raman, with intensity scale five times less than the polarized Raman. The dark and light solid (dash) vertical lines in (E) and (F) are drawn to compare peak positions for E_2 (E_1) to the case of the other enantiomer.

Figure 4

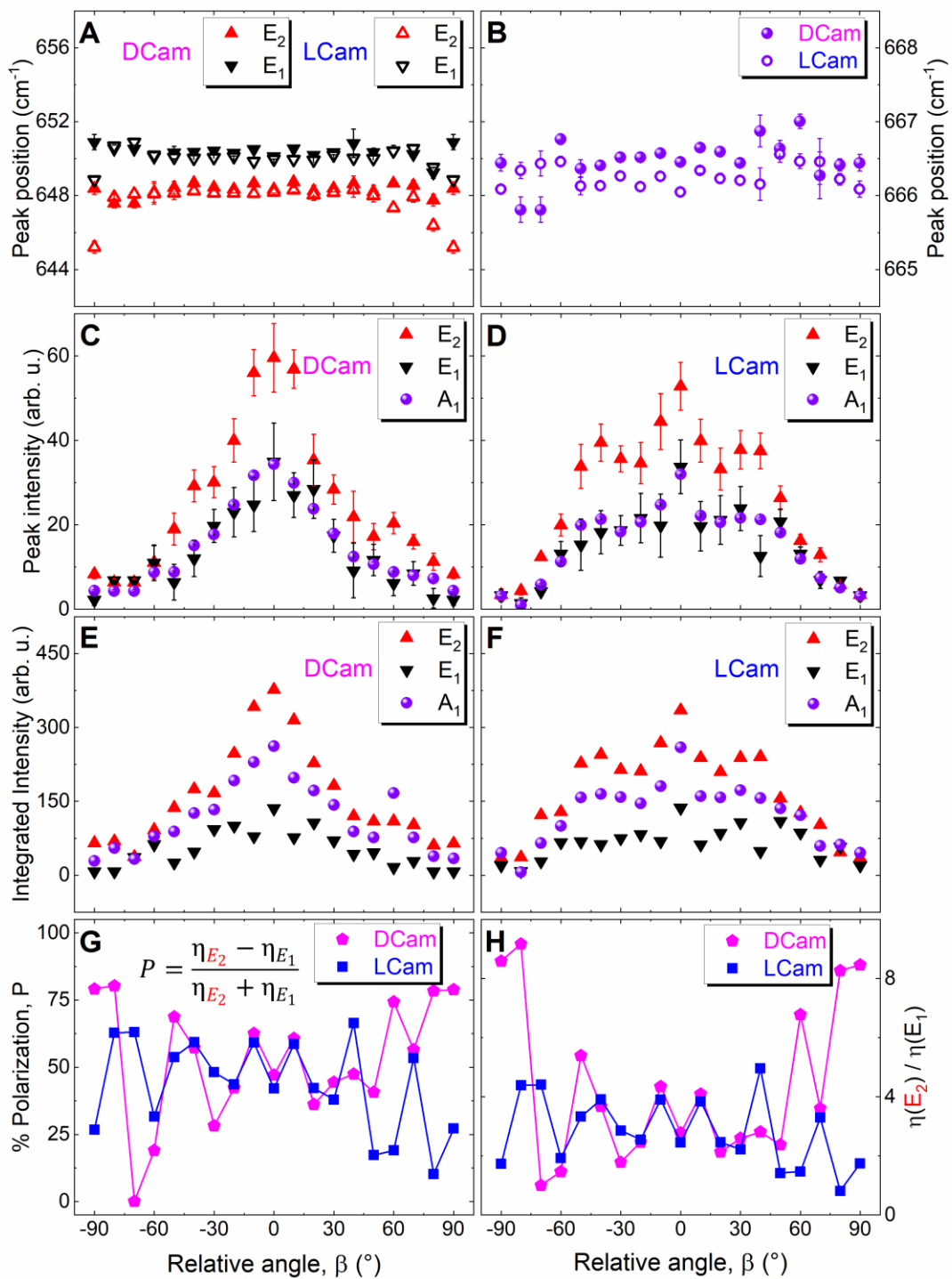


Fig. 4. Chirality dependence of camphor vibronic states. The peak positions extracted from fittings to the Raman spectra (as in Fig. 3, C to F), for (A) the peaks associated with

E_2 and E_1 , and (B) A_1 . Strong redshift (weak blueshift) of both E_2 and E_1 for L (D) camphor in (A) due to the noncoincidence effect. No clear difference was observed for A_1 (B). The peak intensities for E_2 , E_1 , and A_1 extracted from fittings to the Raman spectra (from Fig. 3, C to F), for D camphor (C) and L camphor (D); E_1 and A_1 exhibit similar behavior. The integrated areas for D camphor (E) and L camphor (F); trend of E_2 and A_1 look more alike, while E_1 is weaker, vibronic mode feature and chirality dependence of the PJT states. (G) Integrated areas can be taken as occupancy η , and a polarization between $\eta(E_2)$ and $\eta(E_1)$ is defined, with a clear difference between enantiomers near the depolarized state. (H) $\eta(E_2) > \eta(E_1)$ for the polarized state in both camphor. For D camphor, $\eta(E_2)$ is substantially larger in the depolarized state; while for L camphor, there is only slight decrease towards the depolarized state from the polarized case.

Table 1. Determined values of peak positions and full-width half-maximum (FWHM) of camphor vibronic states for polarized and depolarized Raman spectra. The peak positions (or energies) and FWHM values of the fitting curves at the polarized (Fig. 3C and D) and the depolarized (Fig. 3E and F) Raman spectra are tabulated for the peaks associated with E_2 , E_1 , and A_1 for D and L camphor, respectively.

	Peak position of E_2 (cm^{-1})	Peak position of E_1 (cm^{-1})	Peak position of A_1 (cm^{-1})	FWHM of E_2 (cm^{-1})	FWHM of E_1 (cm^{-1})	FWHM of A_1 (cm^{-1})
DCam polar	648.3 ± 0.2	650.1 ± 0.1	666.5 ± 0.1	4.6 ± 0.2	2.9 ± 0.5	5.8 ± 0.2
LCam polar	648.2 ± 0.2	650.0 ± 0.1	666.0 ± 0.1	4.2 ± 0.2	2.6 ± 0.4	5.4 ± 0.2
DCam depolar	648.4 ± 0.3	650.9 ± 0.4	666.4 ± 0.1	5.8 ± 0.5	3.2 ± 1.6	5.3 ± 0.5
LCam depolar	645.2 ± 1.2	648.9 ± 0.4	666.1 ± 0.3	8.5 ± 3.0	4.7 ± 1.5	13.9 ± 2.1

Supplementary Files

This is a list of supplementary files associated with this preprint. Click to download.

- [SIAppendixDemonstrationofmolecularchiralitydiscriminationbyresonanceRamanscatteringv11.pdf](#)